A Profile-based Estimated Inversion Strength

Zhenquan Wang[1], Jian Yuan[1, *], Robert Wood[2, *], Yifan Chen[1] and Tiancheng Tong[3]

[1] School of Atmospheric Sciences, Nanjing University, Nanjing, China

[2] Department of Atmospheric Science, University of Washington, Seattle, USA

5   [3] Tianwen School, Yichang, China

Correspondence to: Jian Yuan (jiany@nju.edu.cn) and Robert Wood (robwood2@uw.edu)

Abstract. To better measure the planetary boundary layer inversion strength (IS), a novel profile-based estimated inversion strength (EIS_p) is developed using the ERA5 daily reanalysis data. The EIS_p is designed to estimate the IS based on the thinnest possible reanalysis layer above the lifting condensation level encompassing the inversion layer. At the Southern Great Plains

10   site, the EIS_p better correlates with the radiosonde-detected IS (R=0.74) than the lower-tropospheric stability (LTS, R=0.53) and the estimated inversion strength (EIS, R=0.45). And the daily variance in low-cloud cover (LCC) explained by the EIS_p is twice that explained by the LTS and EIS. Higher correlations between the EIS_p and the radiosonde-detected IS are also found at worldwide radiosonde stations.

Analysis on LCC observed by geostationary satellites and the Moderate Resolution Imaging Spectroradiometer shows

15   that the EIS_p explains 78% of the annual mean LCC spatial variance over global oceans and land, larger than that explained by the LTS/EIS (48%/13%). Over tropical and subtropical low-cloud prevailing eastern oceans, LCC range is more resolved by the EIS_p (48%) than the LTS/EIS (37%/36%). And the EIS_p explains a larger fraction (32%) in the daily LCC variance, as compared to that explained by the LTS/EIS (14%/16%). The seasonal LCC variance explained by the EIS_p is 89%, larger than that explained by the LTS/EIS (80%/70%). The relationship between EIS_p and LCC is more uniform across various time scales

20   than the LCC-LTS/EIS relationship. It is suggested that the EIS_p is a better cloud controlling factor for LCC and likely a useful external environmental constraint for process-level studies in which there is a need to control for large-scale meteorology in order to isolate the cloud responses to aerosols on short timescales.

1. Introduction

The inversion strength (IS) of the planetary boundary layer (PBL) is an important factor affecting PBL moisture trapping

25   and low cloud formation. Currently two approximate measures of the IS based on reanalysis data are widely used as meteorological constraints on low cloud cover (LCC): the lower-tropospheric stability (LTS, Klein and Hartmann (1993)) and the estimated inversion strength (EIS, Wood and Bretherton (2006)). They are both defined as a two-level potential temperature (θ) difference between the 700hPa level and the surface but for the EIS the moist adiabatic θ increase above the lifting condensation level (LCL) is removed in addition. The EIS can be combined with the moisture difference between the 700hPa

30   and surface to form a new stability index, the estimated cloud-top entrainment index (ECTEI). The ECTEI and the EIS have similar correlations with LCC on the seasonal time scales (Kawai et al., 2017).

The LTS and EIS are the best known and most widely-used cloud controlling factors to explain LCC variations. Enhanced LTS can moisten PBLs and has been shown to precede LCC changes by about 24-36 hours (Mauger and Norris, 2010; Klein, 1997). Similarly, Myers and Norris (2013) found that the EIS is the main cause of LCC variations and enhanced subsidence

35   actually decreases LCC for the same value of the EIS. This LCC-LTS/EIS relationship is vital for not only separating observational aerosol effects on clouds from meteorological influences (L'ecuyer et al., 2009; Rosenfeld et al., 2019; Murray-Watson and Gryspeerdt, 2022; Coopman et al., 2016) but also estimating low cloud climate feedbacks (Klein et al., 2017; Sherwood et al., 2020). In terms of aerosol-cloud interactions, the LTS and EIS can be used to constrain meteorological

influences and thus largely reduce the confounding influence of meteorology to separate aerosol effects on low clouds (Mauger
40   and Norris, 2007; Coopman et al., 2016), since LCC variations are most explained by the LTS/EIS among all of LCC-
controlling meteorological factors (Stevens and Brenguier, 2009). Without strong cloud-controlling factors, the confounding
influence of meteorology is poorly constrained and over half of the relationship between aerosol optical depth and LCC results
from meteorological covariations (Gryspeerdt et al., 2016). Besides, in climate projections, Webb et al. (2012) found that most
climate models cannot reproduce the observational LCC-LTS/EIS relationship and thus low cloud feedbacks have the largest
45   spread among climate models. To help constrain future climate projections, the LTS/EIS-induced low cloud feedback can be
more accurately estimated by multiplying the observational LCC-LTS/EIS sensitivity by the LTS/EIS changes of climate model
projections (Webb et al., 2012; Qu et al., 2014; Myers and Norris, 2016; Klein et al., 2017; Mccoy et al., 2017; Myers et al.,
2021; Seethala et al., 2015; Kawai et al., 2017).

Although the LTS/EIS is best correlated with LCC among all meteorological factors, the LTS/EIS only explains a small
50   portion of LCC variance on short time scales. 12% of daily LCC variance are explained by the LTS, but when the monthly
means are subtracted from the data only 4.8% of the daily LCC variance are explained by the LTS at the subtropical ocean
weather station (OWS) N (Klein, 1997). Similarly, when the monthly means are removed, only 4% of daily LCC variance are
explained by the EIS over the typical subtropical eastern oceans (Szoeke et al., 2016). This is possibly due to IS not being well
estimated by the LTS and EIS on short time scales.

55   Grounded on the well-mixed condition, the PBL's thermal structure is relatively simple and both the LTS and EIS are
likely good measures of IS. However, the actual PBL thermal stratification may not always be well-mixed. In deep decoupled
PBLs, θ in the subcloud layer may not be conserved but with a stable layer (Jones et al., 2011). In this case, both the LTS and
EIS likely count the stable layers within the PBL into the IS estimates and thus overestimate the real IS atop the PBL. Previous
studies also showed that the free-tropospheric lapse rate has small biases and large spreads although on average it is close to
60   the moist adiabat on daily time scales (Wood and Bretherton, 2006). Thus further refinements on the algorithm of IS estimations
are possible if we can reduce the biases and errors resulting from the deviations from the well-mixed conditions. Given the
importance of the LTS/EIS for studies of cloud-aerosol interactions and climate predictions, a better measure of the IS can lead
to more accurate quantification and increasing confidence in these fields. Based on the previous EIS framework, this study
further establishes a profile-based EIS (EIS_p) algorithm to take advantages of the ERA5 reanalysis and thus more accurately
65   estimate the IS.

This paper is laid out as follows: Section 2 briefly describes the observation and reanalysis data and introduces
methodologies used in our analysis; section 3 illustrates the development and validation of the new EIS_p; section 4 evaluates
the EIS_p on estimating the IS and constraining LCC on global scale; with conclusions in section 5.

2. Data

2.1 Radiosonde and cloud observations at the ARM sites

70   The SGP observatory (97.5ºW, 36.6ºN and 318m above the sea level) is a long-term field measurement site established by
the ARM. In this study, the atmospheric temperature, relative humidity (RH) and pressure profiles measured by the SGP
balloon-borne sounding system (SONDE) from 2002 to 2011 are used. The sondes are launched four times a day at 5:30, 11:30,
17:30, 23:30 coordinated universal time (UTC). To avoid the diurnal-cycle influence on our analysis, only the sondes launched
75   at 17:30 UTC (11:00 local time) are used. At this time, the PBL is relatively more well-mixed by turbulence with more uniform
vertical distribution of θ than the other time of a day (Liu and Liang, 2010). The data at different time are also tested and they
come to similar results. The precision of the sonde-measured temperature, RH and pressure is 0.1K, 1% and 0.1hPa (Ken,
2001), respectively. Their accuracy is 0.2K, 2% and 0.5hPa, respectively (Ken, 2001). Its vertical resolution is normally about
10 meters from the ground level up to 30km. The sonde temporal resolution is less than 2.5s with 6m/s ascent rate at the

80   1000hPa level. The θ profile is computed from the sonde temperature and pressure profiles as:

$$\theta = T(\frac{1000}{p})^{\frac{R_a}{c_{pa}}}, \tag{1}$$

where R_a is the specific gas constant of dry air; c_{pa} is the specific heat capacity for dry air at constant pressures. T and p are the sonde temperature and pressure. The θ vertical gradient $(d\theta/dz)$ profile is derived from the θ difference between two adjacent levels:

85

$$(\frac{d\theta}{dz})_{\frac{z_{i+1}+z_i}{2}} = \frac{\theta_{i+1}-\theta_i}{z_{i+1}-z_i}, \tag{2}$$

where z is the height above the ground level (AGL). The subscript "i" indicates the i-th level detected by the sonde.

Cloud profiles are observed every 10s by the 35GHz millimeter wavelength cloud radar (MMCR) and the micro-pulse lidar (MPL) from 2002 to 2011 at the SGP. The ARM best estimate cloud radiation measurement (armbecldrad) product is used (Chen and Xie, 1996), which provides radar and lidar cloud profiles derived from the Active Remote Sensing of Clouds

90   (ARSCL). Its vertical resolution is 45 meters. To match the sonde launched at 17:30 UTC, the hourly segment of cloud measurements during 17:00-18:00 UTC is used. The cloud base/top height of an hourly segment is recognized as the lowest/highest level of cloud layers (non-zero cloud fraction) detected in that hourly segment. In a cloud profile, distinct cloud layers are separated by a minimum distance threshold of 250m (Li et al., 2011). Low clouds are defined as the cloud base height less than 3km and the top height less than 4km. These low clouds are dominated by stratus, stratocumulus, and shallow

95   cumulus clouds (Dong et al., 2005). Segments of solely other types of clouds but no low cloud are excluded in our analysis. The LCC of an hourly segment is defined as the ratio of the number of cloudy profiles to the total number of profiles in that segment. These hourly segments are further sorted into three categories: clear sky, coupled cloudy and decoupled cloudy segments. Clear sky segments are those in which no cloud is present within that segment. The coupled/decoupled cloudy segments are segments containing low-clouds in coupled/decoupled PBLs, respectively.

100   The ARM Eastern North Atlantic (ENA) atmospheric observatory is located on Graciosa Island (28.1°W, 39.5°N). The ENA site is characterized by marine stratocumulus clouds but at midlatitude oceans where the relationship between LCC and IS is poor and stratus occurs usually with no inversion (Norris, 1998). Our results will further confirm this at the ENA site latter. In contrast, the SGP is a more suitable site than the ENA to study the relationship between LCC and IS. At the SGP, LCC and IS are better correlated with each other than that at the ENA but this LCC-IS relationship is poorly/wrongly reflected

105   by the LTS and EIS according to our results, which outstands the problem of using the LTS and EIS to estimate the IS. Thus in this study we choose to show detailed analysis based on the observations at the SGP site, while the analysis at the ENA site is summarized and listed together with other radiosonde stations in Table 2.

2.2 Worldwide radiosonde stations

The Integrated Global Radiosonde Archive (IGRA) of the National Oceanic and Atmospheric Administration (NOAA)

110   collects radiosondes from global distributed stations (Durre et al., 2018; Durre et al., 2006). The radiosonde temperature, RH, pressure, and geopotential height profiles in the IGRA are used. The θ and θ gradient profiles are computed from Eqs. (1) and (2). These atmospheric parameters of radiosondes are available at the standard pressure levels (1000, 925, 850, 700 and 500hPa) or variable levels. It provides reliable instantaneous observations for the PBL IS (see definitions in the section 2.5). However, most low-cloud dominated regions are over the ocean with no available radiosondes in the IGRA. Thus five radiosonde stations

115   with relatively higher occurrence frequencies of low clouds are selected: the OWS N in the subsidence and steady trade wind circulation of the northeast Pacific (Klein, 1997; Klein et al., 1995); the OWS C in the frequently decoupled PBLs of the north Atlantic (Norris, 1998); the tropical east Pacific coast with the classic stratocumulus condition (Albrecht et al., 1995); the southeast Pacific coast with the stratocumulus-capped PBLs (Bretherton et al., 2004) and the southeast Chinese coast of subtropical low-cloud domains (Klein and Hartmann, 1993). Locations, observational period and time of data for each station

120   are listed in Table1.

Table 1. The location, observational period and time of the IGRA radiosonde stations.

	OWS N	OWS C	Tropical East Pacific coast	Southeast Pacific coast	Chinese coast
Location	(140°W, 30°N)	(35.5°W, 52.75°N)	(120.5667°W, 34.75°N)	(70.4408°W, 23.4503°S)	(119.2833°E, 26.0833°N)
Period	1969-1974	1969-1974	2006-2011	2006-2011	2006-2011
Time	00UTC	12UTC	00UTC	12UTC	00UTC

2.3 GEO-MODIS LCC

Global hourly LCC between 60°S and 60°N derived from geostationary satellites (GEOs) and the Moderate Resolution
125   Imaging Spectroradiometer (MODIS) onboard the Aqua and Terra satellites during 2006-2011 is used. It is available in the
Clouds and the Earth's Radiant Energy System (CERES) synoptic 1-degree (SYN1deg) edition 4.1 product (Doelling et al.,
2013; Doelling et al., 2016; Trepte et al., 2019). The GEO-MODIS LCC here refers to the cloud area fraction of the identified
cloudy pixels with cloud top pressure above 700hPa divided by the total number of pixels in the 1°×1° grids. The MODIS
pixel-level cloud identification is based on the CERES MODIS cloud algorithm (Minnis et al., 2008; Minnis et al., 2011). The
130   sampling frequency of clouds derived from the MODIS narrowband radiance is four times a day (two from each of the Aqua
Terra). GEOs with radiances calibrated against the MODIS provide hourly cloud retrievals between MODIS observations
(Doelling et al., 2013). The GEO cloudy pixel identification is also based on the CERES MODIS-like cloud algorithm to
achieve more uniform MODIS and GEO clouds. An advantage of this product over cloud retrievals of the first-generation GEO
is that the CERES project uses the latest generation of the GEO imager capability with more additional channels to enhance
135   the accuracy of cloud retrievals (Doelling et al., 2016). Hourly LCC is used to match the IGRA radiosondes. Daily LCC used
in section 4 is the mean of the full-day hourly GEO-MODIS LCC from the CERES SYN1deg Ed4.1 product (Doelling et al.,
2016).

2.4 The fifth generation ECMWF atmospheric reanalysis (ERA5)

The European Centre for Medium-Range Weather Forecasts (ECMWF) ERA5 reanalysis combines observations with
140   model outputs by the 4D-Var assimilation to achieve the 1-hour resolution (Hersbach et al., 2020). The hourly atmospheric
temperature, RH, geopotential profiles in the ERA5 dataset are used to match the SGP, IGRA and GEO-MODIS observations.
The θ and θ gradient profiles are computed based on Eqs. (1) and (2). Atmospheric profiles at the 16 pressure levels between
500hPa and 1000hPa are available. At the SGP site, the ERA5 atmospheric profiles between the years 2002 and 2011 at the
grid point (97.5°W, 36.625°N) nearest to the SGP site (away about 2.8km) is used. For the IGRA radiosonde stations, the ERA5
145   hourly data of the 0.125° grid point nearest to them during the same observational period is used. At the global scale, the ERA5
atmospheric profiles are averaged to 1° resolution data centered at 0.5°, 1.5°, … during the years between 2006 and 2011. This
resolution is consistent with the global LCC data. Those three metrics, LTS, EIS and EIS$_p$, are then computed based on the 3-
hour 1° ERA5 atmospheric profiles. All metrices at longer (i.e., from daily to seasonal) time scales are computed from the 3-
hour metrices.

150   **2.5 LTS, EIS and radiosonde-measured IS**

The LTS and EIS over the ocean are defined as:

$$\text{LTS} = \theta_{700hPa} - \theta_0, \tag{3}$$

$$\text{EIS} = \text{LTS} - \Gamma_m (z_{700hPa} - z_{LCL}), \tag{4}$$

where θ and z are, respectively, the potential temperature and the height. The subscripts "700hPa", "0" and "LCL" indicate the levels of 700hPa, 1000hPa and the LCL, respectively. z_{LCL} is calculated using temperature and RH at 1000hPa based on the exact expression in Romps (2017), indicating the height at which an air parcel would saturate if lifted adiabatically. Γ_m is the moist-adiabatic θ gradient at 850hPa calculated using the mean temperature of the 1000hPa and 700hPa levels. Γ_m can be calculated as:

$$\Gamma_m\,(T,p) = (\frac{1000}{p})^{\frac{R_a}{c_{pa}}} \cdot \frac{g}{c_{pa}} (1 - \frac{1+L_v q_s(T,p)/R_a T}{1+L_v^2 q_s(T,p)/c_{pa} R_v T^2}). \tag{5}$$

q_s is the saturated mass fraction of water vapor. L_v is the latent heat of vaporization. R_v is the specific gas constant for water vapor.

Over land, the LTS and EIS are computed following Eqs. (3)-(5) but based on the heights of 0.15km and 3km AGL. The height of the initial air parcel set as 0.15km AGL is to avoid noisy and contaminated readings of the RH near the surface from the radiosondes and the influence of surface layers (Liu and Liang, 2010). The temperature, RH and pressure at 0.15km and 3km AGL over land can be directly derived from the radiosondes or linearly interpolated from the ERA5 profiles. z_{LCL} over land is calculated using the temperature and RH at 0.15km AGL. Γ_m over land is computed using the mean temperature and pressure of the two heights.

To derive the IS from the radiosonde profiles, the layer of the greatest θ gradient ($d\theta/dz$) between the LCL and 5km AGL is firstly identified, similar to Mohrmann et al. (2019) but with a LCL constraint to guarantee that it is above the cloud layer. For the SGP high-resolution (10 meters) radiosondes, the inversion top/base is thus defined as the height of three-fourths of the greatest $d\theta/dz$ above/below the height of the greatest $d\theta/dz$. An alternative method is to define the layer between the identified height of the greatest $d\theta/dz \pm 250$ meters as the inversion layer. These two methods both works. The IS is defined as the θ jumps across the inversion layer after removing the θ increases due to the moist adiabat in this layer:

$$\text{IS} = (\theta_{IST} - \theta_{ISB}) - \Gamma_m^{ISB}(z_{IST} - z_{ISB}). \tag{6}$$

The subscripts "IST" and "ISB" indicate the identified top and base height of corresponding layers, respectively. Γ_m^{ISB} is the moist-adiabatic $d\theta/dz$ computed from Eq. (5) using the temperature and pressure at the identified inversion base. For the low-resolution (hundreds of meters) radiosondes in the IGRA, three candidate layers are identified: a layer corresponding to the greatest $d\theta/dz$ above the LCL and this layer combined with an adjacent layer above or below it. The final IS is selected as the maximum diabatic θ increase of the above three candidate layers computed based on Eq. (6).

2.6 t-test and multiple timescale analysis

In our study the Pearson's correlation coefficient (R) and the slope of the least-squares linear fit are used. R-square is used with a minus/plus sign for a negative/positive correlation. The existence of a correlation and confidence interval for the true mean value (μ) are estimated based on the t-test. The number of independent samples is determined by dividing the total length of samples by the distance between independent samples (Bretherton et al., 1999). All correlations listed in this study are at the 95% significant level if without a mention of their significance. The confidence bound of R is computed based on the Fisher-Z Transformation. The confidence interval of the slope is computed from the residual error of the least-squares linear fit. Besides, for isolating the correlation and the regression slope on different time scales through daily to seasonally, window anomalies are defined in consistent with that in Szoeke et al. (2016):

$$x^{\Delta_i} = [x]^{\Delta_i} - [x]^{\Delta_{i+1}}. \tag{7}$$

The brackets represent mean of x over the window of length Δ. The superscripts Δ_i and Δ_{i+1} are the i-th window length and the next longer window length. The correlation and slope on the different time scales can be computed from the appropriate window anomalies.

3. The profile-based EIS (EIS$_p$)

3.1 Constraining LCC by LTS, EIS and IS at the SGP
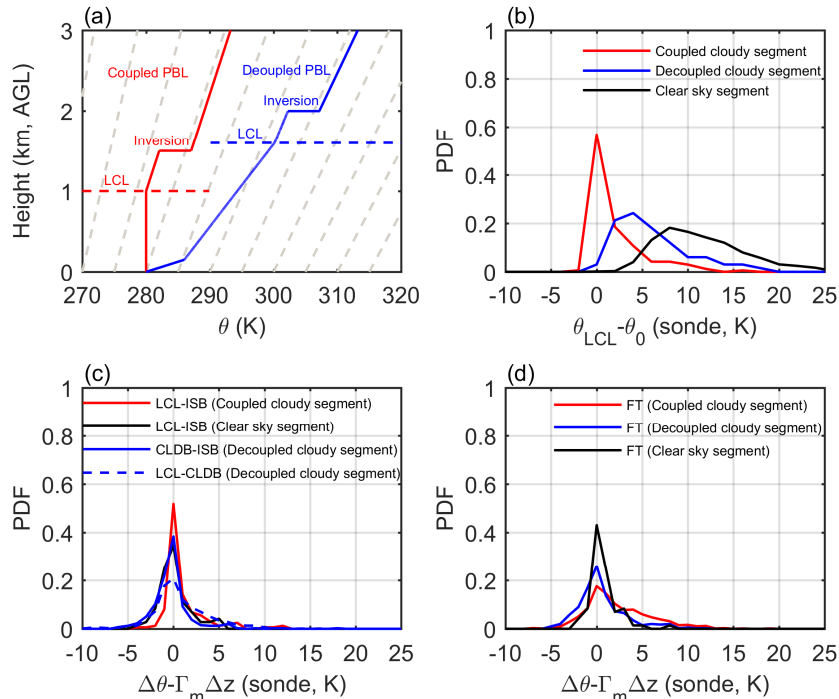
195

Figure 1. Illustrations of PBL θ profiles (a), with the LCL heights indicated by horizontal dash lines and the moist adiabat represented by light dash lines. PDFs of the θ difference between the LCL and 150m AGL (b), the θ difference with the moist adiabat removed between the LCL and the inversion base (c) and the θ difference with the moist adiabat removed for the free troposphere between the inversion top and 3km AGL (d). The red, blue and black lines are for coupled cloudy, decoupled cloudy and clear sky segments, respectively. In (c), the θ differences of decoupled cloudy segments are further separated into that between the LCL and the cloud base (blue dash line) and that between the cloud base and the inversion base (blue solid line).

The characteristics of PBL thermal structures are examined by using the SGP high-resolution radiosondes. Fig. 1a illustrates an idealized θ profile for the coupled PBLs consistent with that of well-mixed conditions in Wood and Bretherton (2006) and an idealized θ profile for the decoupled PBLs based on the observations in Jones et al. (2011). The primary difference in the θ profiles between the coupled and decoupled PBLs is whether a stable layer exists to decouple the cloud and subcloud layers (Nicholls, 1984). Hence, under the decoupled conditions, the LTS and EIS could compute the sum of the PBL IS and the θ increase from the ground to the LCL (Fig. 1a) as the IS estimates. In general, the LTS and EIS can be separated into different terms:

$$\text{LTS} = (\theta_{LCL} - \theta_0) + \Delta\theta + \text{IS}, \tag{8a}$$

$$\text{EIS} = (\theta_{LCL} - \theta_0) + (\Delta\theta - \Gamma_m\Delta z) + \text{IS}, \tag{8b}$$

$$\Delta\theta = \theta_{3km} - \theta_{LCL} - \text{IS}, \tag{8c}$$

$$\Delta z = z_{3km} - z_{LCL}. \tag{8d}$$

The subscripts of "3km", "0" and "LCL" indicate the levels of 3km, 150m AGL and LCL. In Eq. (8a), the LTS can be regarded as the sum of the θ difference between the LCL and 150m AGL ($\theta_{LCL} - \theta_0$), the θ increase ($\Delta\theta$) due to the actual θ gradient above the LCL, and the PBL IS. Similarly in Eq. (8b), the EIS is similar to the LTS except that the θ increase due to the moist-adiabat ($\Gamma_m\Delta z$) above the LCL is removed. It can be seen that the first two terms on the rhs of Eqs. (8a) and (8b) are contributing

to the LTS and EIS even though they are not a part of the IS. In the well-mixed PBLs, the two terms $\theta_{LCL} - \theta_0$ and $\Delta\theta - \Gamma_m\Delta z$

220   are both equal to zero. Thus the EIS defined as Eq. (8b) is exactly the IS and the LTS defined as Eq. (8a) equals to IS $+ \Gamma_m\Delta z$ under perfectly well-mixed conditions.

A straightforward indicator to distinguish coupled and decoupled PBLs is the height difference (Δz) between the cloud base and the LCL. An empirical threshold of Δz is 150 meters corresponding to 0.5K of the θ difference in the subcloud layer (Jones et al., 2011). At the SGP, a similar threshold of Δz equal to 180 meters is set to correspond to 0.5K of the θ difference

225   between the cloud base and the LCL. The coupled/decoupled cloudy segments can be directly distinguished by Δz less/greater than 180 meters. At the SGP site, 29%, 32% and 39% observational samples are classified into the coupled cloudy, decoupled cloudy and clear sky segments, respectively. In Fig. 1b: a) the probability distribution functions (PDFs) of $\theta_{LCL} - \theta_0$ for the coupled cloudy segments peak at zero and have relatively large positive skewness; b) strong stratification below the LCL (large positive $\theta_{LCL} - \theta_0$) frequently occurs in the decoupled cloudy and clear sky segments with mean strength of 6.3K and 11.5K,

230   respectively. Thus the largely positively-biased term $\theta_{LCL} - \theta_0$ would be mistakenly counted into the LTS and EIS in the decoupled cloudy and clear sky segments.

Besides, a premise of using LTS and EIS to measure the IS even in the coupled PBLs is that the lower-tropospheric θ gradient can be predicted by the moist adiabat above the LCL. This moist adiabatic assumption is supported in previous studies but still with some uncertainties on the daily time scales (Stone, 1972; Wood and Bretherton, 2006; Schneider and O'gorman,

235   2008). According to PDFs of the θ difference between the LCL and inversion base or between the inversion top and 3km AGL with the moist adiabat removed ($\Delta\theta - \Gamma_m\Delta z$) above the LCL, θ likely follows the moist adiabat above the LCL (Figs. 1c and 1d) with a peak at zero but all PDFs of $\Delta\theta - \Gamma_m\Delta z$ have broad distributions. The standard deviation of $\Delta\theta - \Gamma_m\Delta z$ above the LCL is about 4K. Note that here the Γ_m is computed using the Eq. (5) but based on the temperature and pressure at the base level of each layer.

240   Typically, the real IS is less than 10K. Thus the term $\theta_{LCL} - \theta_0$ due to the systematic deviations of temperature profiles from the dry adiabat below the LCL could easily overwhelm the real IS in Eqs. (8a) and (8b). As a result, at the SGP site, the decoupled cloudy and clear-sky segments (with weak IS but large $\theta_{LCL} - \theta_0$) are largely mixed with the coupled cloudy segments with strong IS when using the LTS and EIS to sort data. Large values of LTS and EIS may correspond to not just strong IS but also weak IS with strong stratification below the LCL. On short time scales (like the daily scale), the spread of

245   $\Delta\theta - \Gamma_m\Delta z$ (Figs. 1c and 1d) resulting from the θ gradient deviating from the moist adiabat above the LCL could add additional uncertainty into the LTS/EIS. Hence, unphysical or weaker relationships between clouds/moisture and the LTS/EIS might exist.
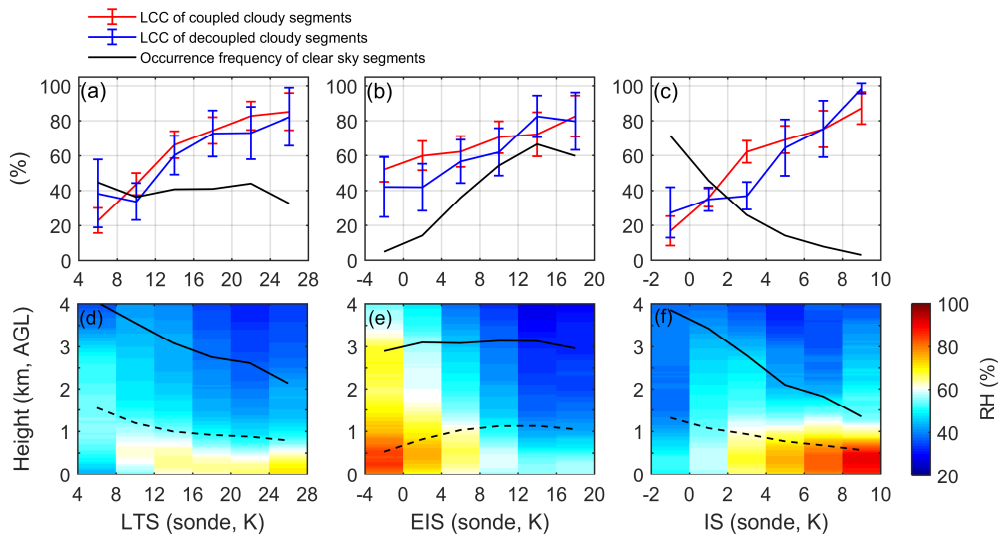
250 Figure 2. Top panel: LCC composites of the coupled cloudy (red line) and decoupled cloudy segments (blue line) and the occurrence frequency of the clear sky segments (black line). Bottom panel: composited RH profiles. Composites are based on the SGP radiosonde-measured LTS (a and d), EIS (b and e) and IS (c and f), respectively. Error bars in (a), (b) and (c) show the 95% confidence interval of the mean based on the t-test. The solid and dash black lines in (d), (e) and (f) indicate the average height of the inversion center and the LCL, respectively. All composites are based on daily data.

255

Figs. 2a-c show that the composited LCC of cloudy segments are all positively proportional to the radiosonde-measured LTS, EIS and IS. However, the composites of LCC are much more sensitive to the changes of IS than the other two estimated metrics. The occurrence frequency of the clear sky segments (the number of clear-sky segments divided by the number of total segments) is investigated separately. Meteorological conditions associated with these hourly segments of no clouds likely

260 extremely disfavor the low cloud formation. Fig. 2c shows that clear sky segments are rarely observed when the IS is very strong (~0% at 10K), and more frequently exist towards weaker IS (60% at 0K). This is consistent with that stronger IS inhibits the entrainment of dry air from the free troposphere and thus favors the formation/maintenance of low clouds and corresponds to less occurrence of the clear sky. On the contrary, such a physically reasonable expectation is not seen (even qualitatively) in the composites based on the LTS and EIS. Figs. 2a-b show that the occurrence frequency of clear sky segments changes little

265 (even increases) with increasing LTS (EIS). This is also expected based on Fig. 1b showing the existence of a large positive skewness in the term $\theta_{LCL} - \theta_0$ in the clear sky segments. This strong static stability below the LCL results in large LTS and EIS even when the real IS is weak.

Composited moisture distribution shows consistent information with the LCC composites. Fig. 2f shows that the composited RH has an increasing trend towards stronger IS and high values of RH (RH>80%) are restricted below 1km at the

270 large IS value bins. However, the composited RH distribution is completely reversed when sorted by the EIS, with high/low RH related to weak/strong EIS (Fig. 2d). The RH distribution sorted by the LTS has similar dependence on the magnitude of the LTS (Fig. 2c) to that on the IS, but with weaker variations and smaller PBL RH as compared to the composites based on the IS (Fig. 2e). Thus the LTS/EIS poorly/incorrectly represents the IS at the SGP site, and hence the dependence of the PBL moisture conditions and LCC on the IS are weakly/wrongly reproduced by the LTS/EIS.
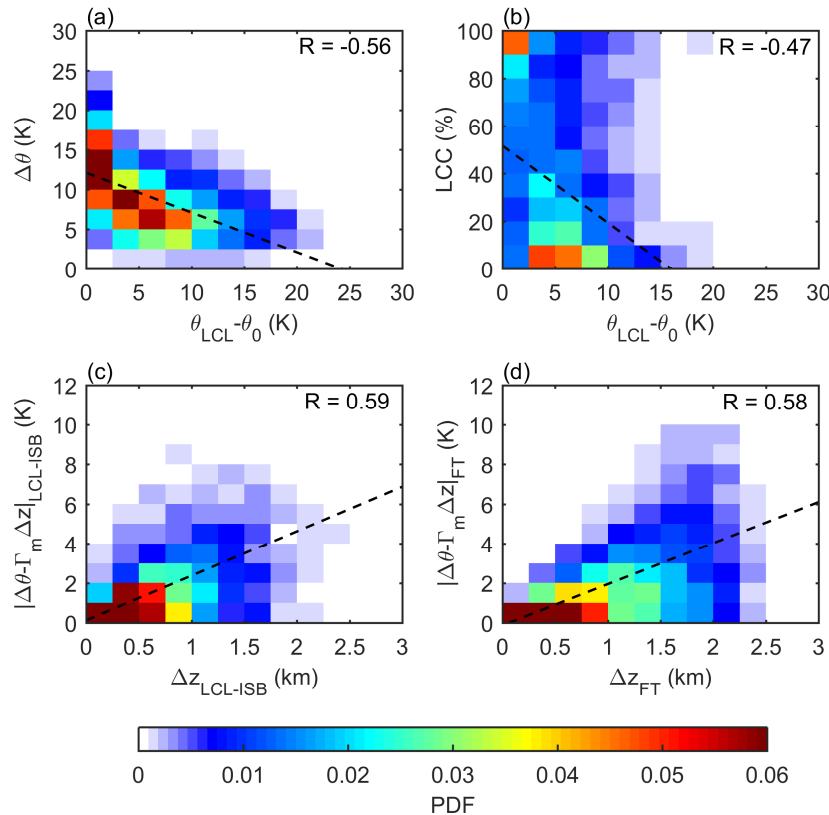
275

Figure 3. Joint PDFs of the θ difference ($\Delta\theta$) between the levels of 3km and the LCL (with the IS excluded) and $\theta_{LCL} - \theta_0$ (a), and PDFs of LCC and $\theta_{LCL} - \theta_0$ (b). Joint PDFs of the absolute value of the θ difference with the moist adiabat removed ($\Delta\theta - \Gamma_m\Delta z$) and the height difference (Δz) from the LCL to the inversion base (c) and from the inversion top to 3km in the free troposphere (d). Correlation coefficients (R) are listed on the upper-right corner of each panel. The black dash lines indicate
280 the least-squares fit.

An interesting phenomenon is that the LTS overall performs better than the EIS with respect to constraining LCC at the

SGP site. To understand why this happens, the LTS and EIS in Eq. (8) both have been separated into three terms to discuss.

For the LTS, the two terms $\theta_{LCL} - \theta_0$ and $\Delta\theta$ of Eq. (8a) usually offset each other with a negative correlation of -0.56 and a

285   slope of the least-squares fit -0.5K/K (Fig. 3a). Thus, the LTS equation can be transformed into:

$$\text{LTS} \approx \left(1 + \frac{\Delta\theta}{\theta_{LCL} - \theta_0}\right)(\theta_{LCL} - \theta_0) + \text{IS}. \tag{9}$$

According to the offset of those two terms, the coefficient of $\theta_{LCL} - \theta_0$ in Eq. (9) is ~0.5. This means that the biases added to

the LTS is about a half of that for the EIS defined as Eq. (8b). Fig. 3b shows that the term $\theta_{LCL} - \theta_0$ is negatively correlated

(a correlation of -0.47) with LCC in contrast to the positive LCC-IS correlation. Thus if large deviations from the dry adiabat

290   below the LCL exist, the LTS actually is a better measure of IS than the EIS, since less biases resulting from the term $\theta_{LCL} -$

θ_0 are involved in the computation of LTS. As shown in Fig. 2, the LTS has positive but relatively weak correlations with the

LCC and RH, but the EIS is negatively correlated with them.

As shown in Figs. 1c and 1d, the θ difference between the actual environmental θ gradient and the moist adiabatic θ

gradient ($\Delta\theta - \Gamma_m\Delta z$) is another source of uncertainty in the EIS based on Eq. (8b), especially on short time scales. However,

295   Figs. 3c and 3d suggest that the spread of $|\Delta\theta - \Gamma_m\Delta z|$ increases with the layer thickness either between the LCL and the

inversion base or between the inversion top and 3km AGL (with a correlation of 0.59 or 0.58, respectively). This is because

that the term $\Delta\theta - \Gamma_m\Delta z$ can also be written as $(\Gamma - \Gamma_m)\Delta z$, where Γ is the environmental θ gradient. This suggests a possible way of reducing uncertainties in estimating the IS if we can reduce the layer thickness (Δz) associated with the second term on the rhs of Eq. (8b) when using it to estimate the IS.

300   **3.2 The algorithm of the new EIS$_p$ and its relationship with LCC at the SGP**
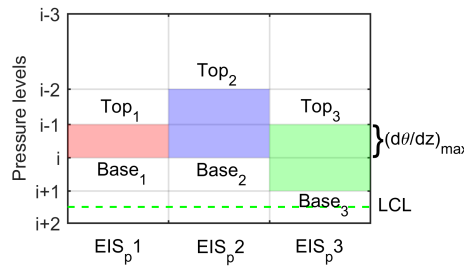
Figure 4. An illustration of finding the location of three possible layers encompassing the inversion in one ERA5 profile. The red block refers to one single ERA5 layer. The blue and green each refers to a combination of two adjacent ERA5 layers. Three candidate EIS$_p$s (EIS$_p$1-3) are computed accordingly.

305

Above results suggest that there are two major bias and error sources of estimating the IS using the LTS and EIS metrics. One is caused by systematic deviations from the dry adiabat below the LCL, the other is the errors resulting from the spread of the actual θ gradient around the moist adiabat above the LCL. To exclude the former source, we can simply locate the LCL to drop the first term on the rhs of Eq. (8b). The impacts of the latter one can be indirectly reduced by reducing the layer

310   thickness that is involved in the computation of the second term on the rhs of Eq. (8b). Specifically, we construct a profile-based IS estimate (EIS$_p$):

$$\text{EIS}_p = (\Delta\theta - \Gamma_m\Delta z) + \text{IS}, \qquad (10a)$$

$$\Delta\theta = \theta_{top} - \theta_{base} - \text{IS}, \qquad (10b)$$

$$\Delta z = z_{top} - z_{base}, \qquad (10c)$$

315   where subscripts "top" and "base" represent the top and base levels for computing the EIS$_p$. Instead of using the two fixed levels in the LTS and EIS, the top and base levels of the inversion layer in the EIS$_p$ are determined by scanning the ERA5 profiles above the LCL. Fig. 4 illustrates how to find the top and base levels of three possible layers encompassing the inversion. One possible layer is the layer corresponding to the maximum $d\theta/dz$ (red zone). Other two possible layers are the blue and green zone referring to the combination of the layer of maximum $d\theta/dz$ and the layer just above or below it, respectively. After

320   finding the targeted layers, three candidate EIS$_p$s are computed using Eq. (10) and the largest one among three is selected as the EIS$_p$.

By this method, the term $\theta_{LCL} - \theta_0$ in the LTS and EIS is completely removed in the EIS$_p$. The term $\Delta\theta - \Gamma_m\Delta z$ in the EIS is reduced according to Figs. 3c and 3d, since the thickness of the layer involved in the computation of the LTS/EIS (from the LCL to 3km) is reduced to about 0.3~1km in the EIS$_p$. This method is suitable for the PBLs with a dominant inversion

325   when used with the ERA5 reanalysis. If multiple inversions with comparable strength occur, this method may not always find the strongest inversion especially if the strongest inversion is distributed into two reanalysis layers. Because this method is designed to find the inversion above the LCL and this height constraint directly filters out the possible large stability below the LCL (e.g., surface-based inversion or decoupled layers), the occurrence of strong secondary inversions is likely rare.
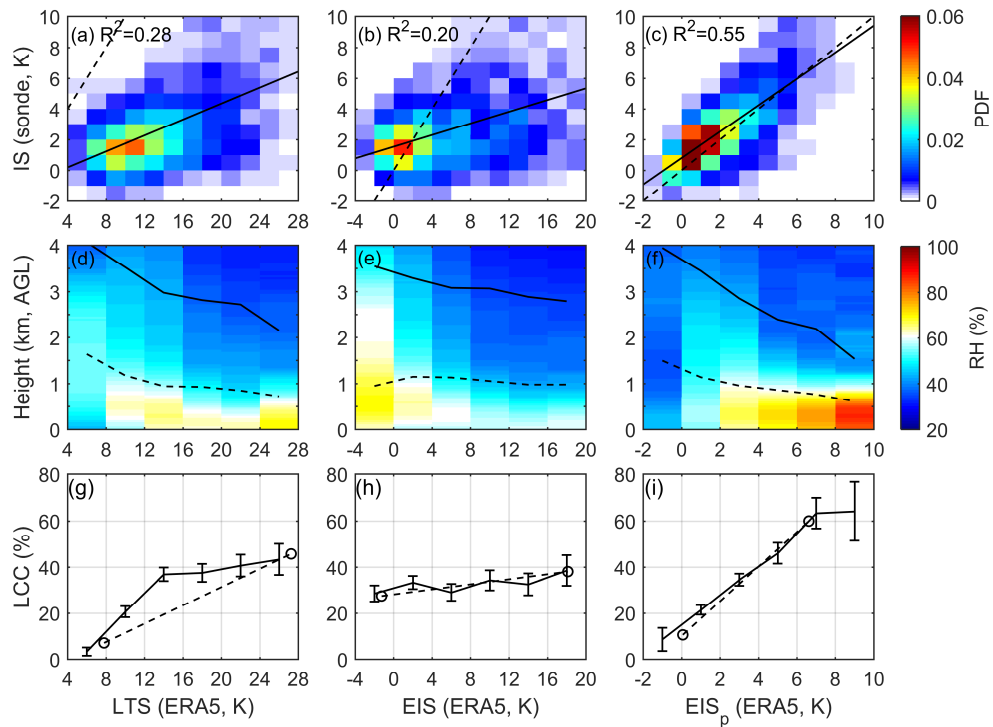
Figure 5. Joint PDFs of the SGP radiosonde-measured IS, and the ERA5-derived LTS (a), EIS (b) and EIS_p (c), respectively. In (a)-(c), the black solid line is the least-squares fit and the dash line is the reference line of y=x. The composites of the radiosonde RH profiles based on the ERA5-derived LTS (d), EIS (e) and EIS_p (f). The black solid and dash lines in (d-f) are the heights of the IS and the LCL, respectively. The LCC composited based on the LTS, EIS and EIS_p are shown in (g), (h) and (i), respectively. The cycles in (g), (h) and (i) corresponds to the 5% and 95% quantile of LTS, EIS and EIS_p and the composited value of LCC in the bins of the smallest and largest 10% of LTS, EIS and EIS_p values. Error bars in (g-i) show the 95% confidence interval of the mean based on the t-test.

The LTS, EIS and EIS_p derived from the ERA5 reanalysis are directly compared against the SGP radiosonde-measured IS. In Fig. 5c, the R-square between the EIS_p estimated from the ERA5 and the IS measured by radiosondes is 0.55, which is much larger than that of the LTS (0.28, Fig. 5a) and EIS (0.20, Fig. 5b). The slope of the least-squares fit of the IS to the EIS_p is 0.86K/K. This indicates the range of the EIS_p is much close to that of the IS as compared to that of the LTS (0.26K/K) and EIS (0.19K/K). The composites of LCC and RH based on the EIS_p (Fig. 5f) show similar results to that based on the IS (Fig. 2f). Stronger EIS_p corresponds to larger RH trapped below about 1km, while decreasing RH (but penetrating to higher levels) with weakening and lifting inversion layers. However, the LCC and RH composites based on the LTS and EIS (Figs. 5d, 5e, 5g and 5h) show weak or wrong relationships similar to the results based on the radiosonde-measured LTS and EIS (Fig. 2a, 2b, 2d and 2e). Thus the EIS_p does a better job on estimating the IS and better constrains the PBL moisture distribution and LCC. The slope of the composited LCC to the EIS_p is 6%/K, in contrast to that to the LTS (1.9%/K) and the EIS (0.4%/K). Since the range of the LTS and EIS is larger than that of the EIS_p, larger slopes of the LCC to the EIS_p than that to the LTS and EIS are expected. To measure the sensitivity of LCC to changes of LTS, EIS and EIS_p, we consider the effective range of LCC resolved by changes in a metric. The sensitivity of LCC to a metric here is defined as the difference between the composited LCC values associated with the largest and smallest 10% of that metric:

$$LCC\ Sensitivity\ to\ x = \overline{LCC(x \geq x_{90\%})} - \overline{LCC(x \leq x_{10\%})}. \tag{11}$$

The bar over the LCC head represents the mean value of LCC sorted by x quantile. $x_{90\%}$ and $x_{10\%}$ are 90% and 10% quantile of x. The LCC sensitivity of all segments to the EIS_p is 50%, which is larger than the LTS (39%) and EIS (12%). These weaker

355   dependences of LCC on the LTS/EIS are expected since large errors (Figs. 1b-1d) are carried in when the IS is estimated by the LTS/EIS. Although the relatively lower vertical resolution of the ERA5 profiles may not always suffice to resolve the inversion layer, the IS estimated from the ERA5 profile-based algorithm is highly consistent with the IS derived from the SGP 10m-resolution radiosondes and they present similar relationships with the PBL RH and LCC.
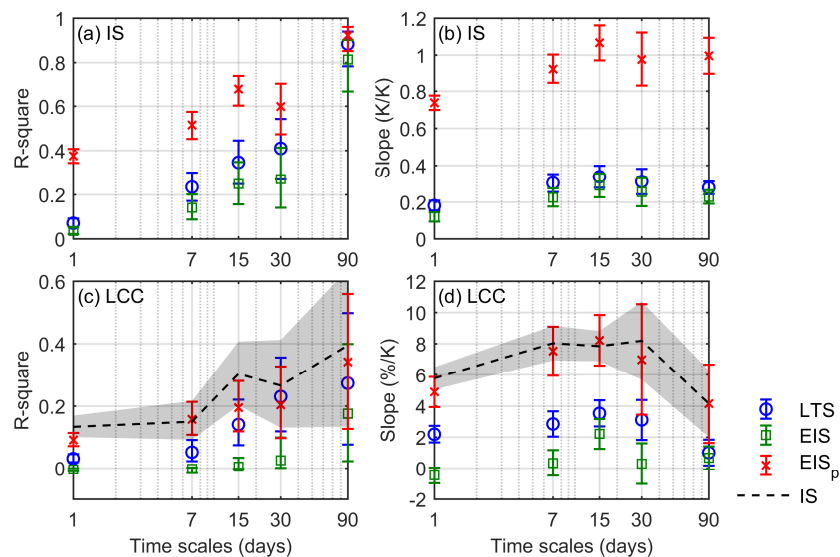
360   Figure 6. R-square (a) and slope of the least-squares fit (b) of the SGP radiosonde-derived IS to the ERA5 reanalysis-based LTS (blue cycle), EIS (green square) and EIS$_p$ (red cross) on daily, 7-day, 15-day, 30-day and 90-day time scales, respectively. R-square (c) and slope (d) of LCC to the LTS, EIS, EIS$_p$ and IS (black dash line) on daily to seasonal time scales, respectively. Error bars and shadows show the 95% confidence interval of the mean based on the t-test.

365   The ERA5-based LTS, EIS and EIS$_p$ are further examined on the different time scales with respect to their relationships with radiosonde-measured IS and LCC (Fig. 6). Overall, the R-square and the slope between the EIS$_p$ and the IS are the largest through all time scales. Particularly on the daily, 7-day and 15-day time scales, the lower bounds of the 95% confidence interval of the EIS$_p$-IS R-square are much higher than the upper bounds for the LTS and EIS. On the seasonal time scale, three metrics have similar correlations with the IS, but as shown in Fig. 6b, the slope of the IS to the EIS$_p$ (nearly 1) is still much larger than

370   that to the LTS (0.28K/K) and EIS (0.23K/K). The limited accuracy restricts the LTS and EIS to reproduce the relationship between the true IS and LCC. In Fig. 6c, on daily time scales, the LTS explains 3.1% of variance in LCC, which is comparable to the 4.8% explained variance by the LTS at OWS N (a typical low-cloud dominated site over the ocean) in Klein (1997). For the EIS$_p$, it explains 9.1% of the daily LCC variance, not bad as compared to that explained by the IS (12-13%). Similar conclusions can be drawn from weekly time scales. On longer time scales, the EIS$_p$ and the LTS both explain comparable

375   variance in LCC but much larger than that explained by the EIS. In Fig. 6d, the slope of LCC composited based on the IS is nearly reproduced by the EIS$_p$ consistently. The slopes of LCC composited based on the LTS and EIS are much smaller than that based on the EIS$_p$ and IS.

4. Evaluation of the LTS, EIS and EIS$_p$ at the global scale

4.1 At worldwide radiosonde stations

380
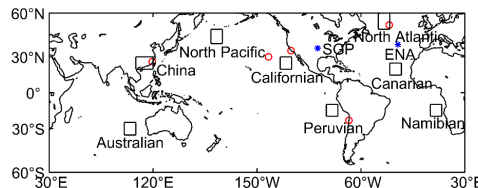
Figure 7. Blue asterisk marks the SGP and ENA sites. Red cycles mark the locations of radiosonde stations from the IGRA. Eight 10º×10º boxes are the most typical low-cloud dominated regions defined in Klein and Hartmann (1993).

385

Table 2. The characterestics of the PBL thermal strucures, evaluation of the LTS, EIS and EIS$_p$ on estimating the IS and the IS-LCC relationships of the six radiosonde stations. Italic indicates not significant correlations. Bold indicates the largest correlation. The daily IS-LCC correlation is based on the dataset excluding 7-day means.

	ARM SGP	ARM ENA	OWS N	OWS C	Tropical East Pacific Coast	Southeast Pacific Coast	Chinese Coast
θ_{LCL}-θ_0 in coupled PBLs (standard deviation)	0.33K (0.36K)	0.26K (0.39K)	1.33K (0.74K)	0.85K (0.86K)	0.70K (1.34K)	0.17K (0.28K)	0.16K (0.93K)
θ_{LCL}-θ_0 in decoupled PBLs (standard deviation)	8.69K (5.82K)	2.55K (2.37K)	3.53K (2.23K)	2.73K (2.30K)	10.46K (6.71K)	1.41K (2.05K)	3.34K (3.50K)
$\Delta\theta - \Gamma_m\Delta z$ above the LCL (standard deviation)	1.22K (3.98K)	0.07K (1.64K)	-0.39K (2.26K)	1.65K (2.74K)	-1.06K (2.36K)	0.48K (2.34K)	-1.16K (2.93K)
IS-LTS correlation	0.53	0.51	0.35	0.29	0.43	0.62	0.62
IS-EIS correlation	0.45	0.58	0.41	0.36	*-0.06*	0.53	0.76
IS-EIS$_p$ correlation	**0.74**	**0.76**	**0.60**	**0.48**	**0.75**	**0.74**	**0.79**
IS-LCC daily correlation (slope ± confidence intervals)	0.34 (2.82 ± 0.42%/K)	0.16 (3.05 ± 0.97%/K)	NAN	NAN	0.26 (2.61 ± 0.43%/K)	0.30 (2.71 ± 0.39%/K)	0.16 (3.07 ± 0.85%/K)
IS-LCC monthly correlation (slope ± confidence intervals)	0.65 (3.65 ± 0.78%/K)	0.43 (6.44 ± 3.34%/K)	NAN	NAN	0.38 (6.95 ± 4.02%/K)	0.71 (4.52 ± 1.06%/K)	0.76 (6.57 ± 1.38%/)

As shown in section 3, at the ARM SGP site, the EIS$_p$ does work better than both the LTS and EIS on estimating the PBL IS when the PBL thermal structure is largely deviated from the idealized structure of well-mixed PBLs. Next, we want to see

390 if such a deviation exists globally. The ARM ENA site and other five ground-based radiosonde stations are selected to examine their characterestics of PBL thermal strucures. Their locations are shown in Fig. 7. Because the cloud base height information is not available, the coupled and decoupled PBLs now are determined by the α_θ:

$$\alpha_\theta = \frac{\theta_{ISB}-\theta_0-\Gamma_m(z_{ISB}-z_{LCL})}{\theta_{IST}-\theta_0-\Gamma_m(z_{IST}-z_{LCL})} = \frac{\theta_{LCL}-\theta_0+[\theta_{ISB}-\theta_{LCL}-\Gamma_m(z_{ISB}-z_{LCL})]}{IS+\theta_{LCL}-\theta_0+[\theta_{ISB}-\theta_{LCL}-\Gamma_m(z_{ISB}-z_{LCL})]}.$$ (12)

The subscripts "ISB", "IST", "0" and "LCL" indicate the base and top of inversion layers, the 1000hPa level and the LCL,

395 respectively. α_θ expresses the decoupling degree and is similar to that defined in Wood and Bretherton (2004), by removing the moist-adiabatic θ increase above the LCL. In perfectly coupled conditions, the numerator of Eq. (12) should be zero. Otherwise, the decoupling degree is in proportion to α_θ. In the tropical and subtropical well-mixed regions, the median value of α_θ is usually less than about 0.2 (Wood and Bretherton, 2004) and thus a threshold of α_θ here is set as 0.2 to distinguish the coupled/decoupled PBLs.

400 As shown in Table 2, it is found that the two terms $\theta_{LCL} - \theta_0$ and $\Delta\theta - \Gamma_m\Delta z$ in Eq. (8) are non-negligible even over the subtropical oceans. Both the mean and standard deviation of $\theta_{LCL} - \theta_0$ are very small in the coupled PBLs. The mean of $\theta_{LCL} - \theta_0$ at the other sites in the decoupled PBLs is usually smaller (about 1-4K) as compared to that at the SGP (8.69K), except at the tropical east Pacific coast, which is larger (10.46K) than that at the SGP. Theoretically, a constant shift on the θ difference between the LCL and the ground level will not change the correlation coefficient and regression slope between the

405   LTS/EIS and the IS/LCC. However, the term $\theta_{LCL} - \theta_0$ is systematically different between the coupled and decoupled PBLs. Thus using the LTS and EIS to sort the PBL structures will unequally mix the coupled and decoupled conditions in their different composite bins. Moreover, this bias is distinct for different places and thus the regional difference would make the LTS and EIS not uniform for their accuracies of estimating the IS. In contrast, this will not happen in the EIS_p since this bias caused by the term $\theta_{LCL} - \theta_0$ in the LTS and EIS is completely excluded from the EIS_p.

410   The standard deviation of the term $\Delta\theta - \Gamma_m\Delta z$ as shown in Table 2 suggests that the errors of estimating the IS based on Eq. (8) due to the moist adiabatic assumption above the LCL of the ENA and other five radiosonde sites range from 57%-74% of that of the SGP site (3.98K). Thus the term $\Delta\theta - \Gamma_m\Delta z$ at these six sites will likely also be reduced when measuring the IS by the EIS_p. Thus it is not surprising that the ERA5 EIS_p is best correlated with the IS directly derived from the radiosondes over all stations (Table 2). Regional differences of the correlations with the IS still exist for all metrics to measure the IS but

415   are relatively small for the EIS_p.

4.2 Relationship between global LCC and LTS, EIS and EIS_p
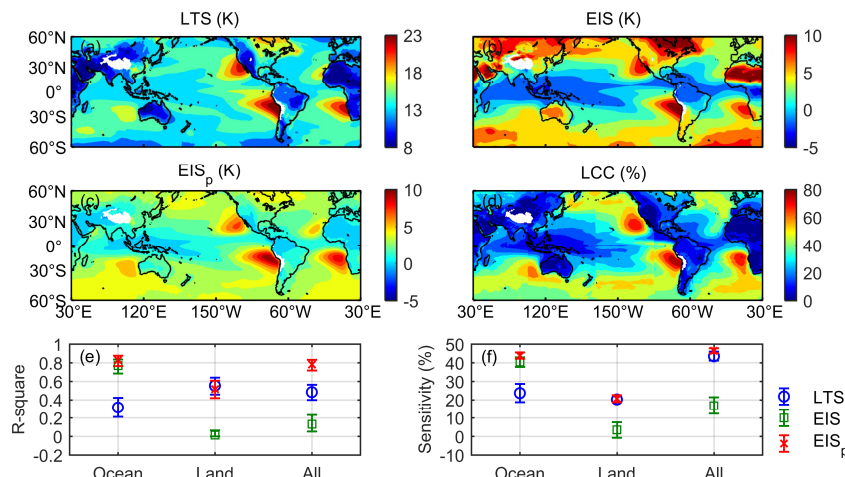
Figure 8. Spatial distribution of the ERA5 reanalysis-based LTS (a), EIS (b), EIS_p (c) and the GEO-MODIS LCC between 60ºS and 60ºN. The specific R-square and LCC sensitivity to the LTS (blue cycle), EIS (green square) and EIS_p (red cross)
420   over the ocean, land and all is shown in (e) and (f), respectively. The error bars show the 95% confidence interval of the mean based on the t-test.

Fig. 8 shows the six-year mean map of the ERA5-based LTS, EIS and EIS_p. The GEO-MODIS LCC global pattern is also used to examine its spatial correlation with the above three metrics. For the EIS_p, the plateau regions with the surface pressure
425   smaller than 700hPa are not investigated here, where no GEO-MODIS LCC is observed. Over the ocean, the EIS_p distribution better corresponds to the pattern of LCC and explains 83% of its spatial variance, higher than that explained by the EIS (77%) and the LTS (31%). Particularly, the locations of the five subtropical strongest EIS_p centers over the eastern oceans are relatively away from the coast (Fig. 8c). This is consistent with the locations of corresponding large LCC centers. In contrast, the centers of strong LTS (Fig. 8a) and EIS (Fig. 8b) are usually over the west coasts, slightly shifting away from those centers
430   of LCC, though these places are usually regarded as the most likely well-mixed PBLs. Over the midlatitude ocean, it is also noted that the LTS value is too small to explain large LCC, and the EIS value is comparable to that over the subtropics but corresponds to LCC much less than the subtropical LCC. Compared with the LTS and EIS, the distribution of EIS_p over global oceans more reasonably explains the LCC spatial variations. Over land, the EIS_p and LTS distribution still well corresponds to the LCC pattern and explains over half of the LCC spatial variance. This implies the IS is still a possible controlling factor for
435   LCC over land and thus accurately estimating the IS over land is also necessary to explain continental LCC variations. But the

EIS over land does a much worse job in most areas and only explains 2% of the spatial variance of LCC. The exact reason of this phenomenon is not known, but seems the poor fault tolerance of the EIS on the term $\theta_{LCL} - \theta_0$ as shown in section 3 might be one reason. The LTS cannot well explain the oceanic spatial LCC variations and the EIS cannot well explain the continental spatial LCC variations. But these will not happen with the EIS_p. Over global oceans and land, the EIS_p explains 78% of the

440   spatial variance in LCC, significantly higher than that explained by the LTS (48%) and EIS (13%). The spatial variations of LCC are also more sensitive to the EIS_p (Fig. 8f).
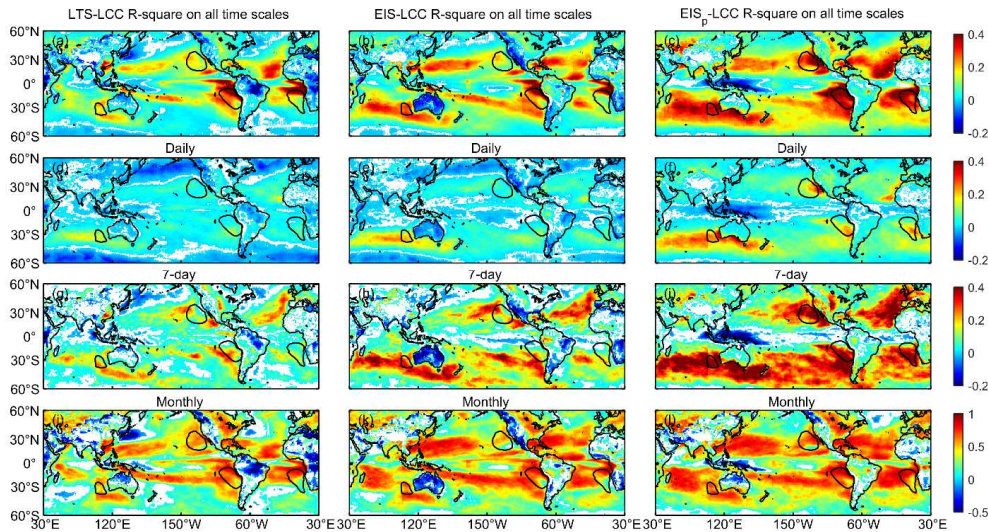
Figure 9. R-square between the GEO-MODIS LCC and the ERA5 reanalysis-based LTS (left column), EIS (middle column) and EIS_p (right column) at the all-time scales (a, b and c), daily time scale (d, e and f), 7-day time scale (g, h and i) and monthly
445   time scale (j, k and l). The black contours enclose regions with LCC larger than 60%. Only correlations at the 95% significant level are shown.

The dependence of LCC on the three ERA5-based metrics is further examined globally on different time scales. On all time scales, the EIS_p explains larger temporal variance in LCC than the LTS and EIS over most places including those typical
450   low cloud prevailing subtropical eastern oceans (Figs. 9a-c). Over the regions with more than 60% of LCC, the EIS_p explains 36% of the variance in LCC on average, much larger than that explained by the LTS (21%) and EIS (20%). The mean LCC sensitivity (defined in Eq. (11) and not shown in figure) to the EIS_p is 48% over these regions, larger than that to the LTS (37%) and EIS (36%). The EIS_p explains larger LCC variance than the LTS and EIS through all time scales (Figs. 9d-i).

Over oceans, the tropical and subtropical LCC is most positively correlated with the three metrics on all of time scales.
455   However, over midlatitude oceans, much weaker or not significant correlations between LCC and the three metrics exist though the annual mean LCC is no less than 40%. The IS and LCC measured by the ARM ENA radiosondes and ground-based instruments also shows a weak IS-LCC correlation (see Table 2) although the ENA site is a midlatitude oceanic site characterized by stratocumulus clouds. This suggests that the IS-LCC relationship is not uniform but varying with regions even over oceans. When the IS is used to constrain the environmental influence on LCC variations, it should be noted that
460   LCC is not all equally constrained by the IS for different regions. For some regions such as midlatitude oceans, the IS might not be a good constraint on LCC. But by more accurately estimating the IS than the LTS and EIS, the EIS_p is more correlated with LCC over either subtropical oceans such as Californian or midlatitude oceans such as North Pacific.

For land regions with relatively more LCC such as the SGP, China and Russia, the correlation between EIS_p and LCC is comparable to the subtropical oceanic regions through all time scales. This suggests the EIS_p is also an important controlling
465   factor for continental LCC over these regions. Although EIS_p is more correlated with LCC variations than the LTS and EIS

over most land regions, over China the LTS explains larger LCC variance than the EIS and EIS$_p$ in Fig. 9a-c. Over China, as shown in Table 2, the LTS-LCC correlation is even larger than the IS-LCC correlation but it is the worst estimation for the IS. This implies that the high correlation of LTS with LCC does not come from the impact of IS controlling LCC but the exact reason behind this is not known.
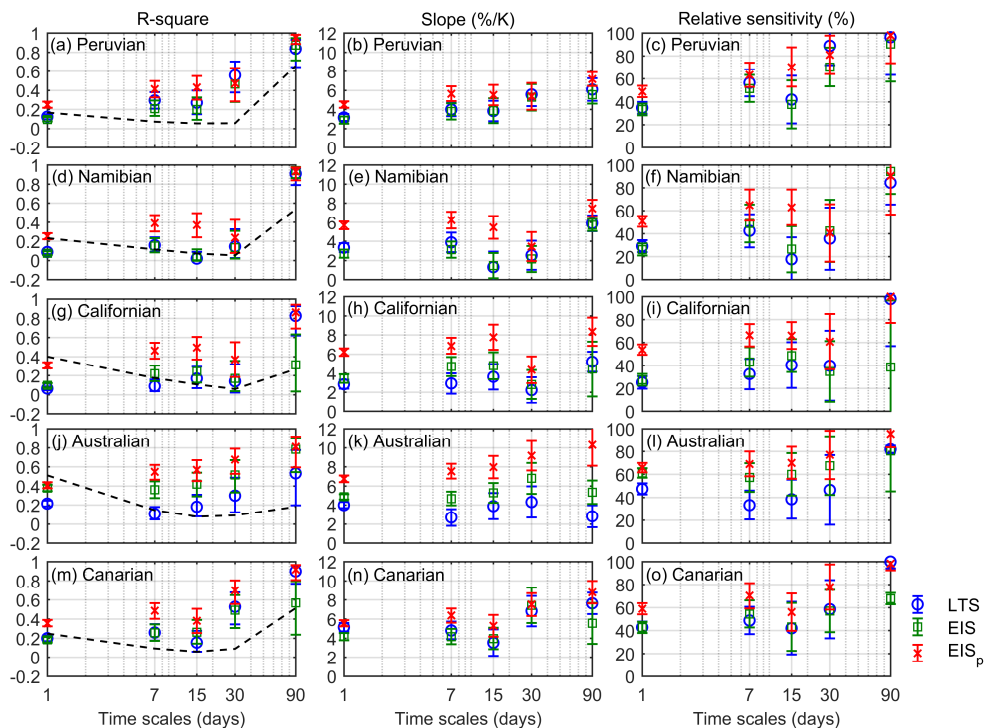
470

Figure 10. R-square (left panel), slope (middle panel) and relative sensitivity (right panel) of the GEO-MODIS LCC to the ERA5-based 10º×10º regional mean LTS (blue cycle), EIS (green square) and EIS$_p$ (red cross) through daily to seasonal time scales over the five typical eastern oceans defined in Klein and Hartmann (1993). The error bars show the 95% confidence interval based on the t-test. The black dash lines in the left panel are the fraction of the LCC variance on different time scales divided by the total variance.

475

In Klein and Hartmann (1993), several key low cloud regions are defined. Those regions are of a particular interest in climate projections due to their strong low cloud albedo effects. As shown in Fig. 7, we pick eight key low cloud regions according to Klein and Hartmann [1993] and the linear relationships between LCC and the three metrics are investigated. These regions lack radiosondes for long-term observations of IS. They are separated into a group of five typical tropical and subtropical low cloud prevailing eastern oceans and a group including midlatitude oceans and subtropical land.

480

As shown in Fig. 10, over the five key tropical and subtropical eastern oceans, the LCC variance comes from all of time scales but with relatively larger portions on daily and seasonal time scales. Over the Peruvian, Namibian and Canarian regions, over 50% of LCC variance are from the seasonal variations and much smaller LCC variance is from other four shorter time scales. But over the Californian and Australian regions, 40% and 51% of the LCC variance are from the daily time scale, larger than that on other time scales. Although the LCC variance on the 7-day, 15-day and monthly time scales are relatively smaller, the sum of them still accounts for about 20~30% of the total LCC variance.

485

In Fig. 10, the LCC variance explained by the LTS, EIS and EIS$_p$ and the slopes of composited LCC to them are examined through daily to seasonal time scales. Besides, the relative LCC sensitivity to those three metrics is defined as the LCC sensitivity divided by the LCC range. Here the LCC range refers to the difference between the mean values of the largest and the smallest 10% of LCC. The LCC variance is most explained by the EIS$_p$ among the three metrics (left panel of Fig. 10) and

490

LCC is most sensitive to the EIS_p (right panel of Fig. 10) through all of these time scales, except the monthly time scale over the Peruvian region and the seasonal time scale over the Namibian. On the daily time scale, 32% of LCC variance are explained by the EIS_p on average over the five eastern oceans, which is more than twice of the variance explained by the LTS (14%) and

495   EIS (16%). On the longer time scales (30-90 days), overall the EIS_p explains 89% of the LCC seasonal variance on average over the five eastern oceans, in contrast to 80% for the LTS and 70% for the EIS. However, the EIS_p robustly explains more than 80% of the seasonal variance in LCC over all places, while the EIS cannot well explain that over the Californian and Canarian regions, as well as the LTS cannot well explain that over the Australian region.

It is also noted that the slopes of the composited LCC associated with each metric are not uniform cross these key low

500   cloud regions or on different time scales. A similar regional and temporal difference is also found in the LCC-IS relationships (Table 2). Klein et al. (2017) and Szoeke et al. (2016) also found the LCC slopes to the LTS/EIS is variant on different time scales and this time-scale dependence would lead to uncertainties in the final estimates of low-cloud feedbacks. Thus the error estimates of the LCC slopes to the LTS, EIS and EIS_p are needed for the final uncertainty estimates of low-cloud feedbacks. To quantify the relative variation (or the uniformness) of the LCC slope to LTS, EIS and EIS_p, we compute the ratio between

505   the standard deviation and the mean of grouped slopes. For the temporal relative variation, over each region slopes on different time scales are grouped together. While for the regional relative variation, on each time scale slopes over different regions are grouped together. The temporal relative variation of the LCC slope to the LTS and EIS is 32% and 29% on average over the five eastern oceans. In contrast, the temporal relative variation of the LCC slope to the EIS_p is 21%. Besides, the regional relative variation of the LCC slope to the LTS, EIS and EIS_p is 24%, 21% and 18% between the five eastern oceans, respectively.

510   This suggests that the regional/temporal dependence of the LCC slope in the estimate of low cloud feedbacks is also non-negligible and needs to be considered in the final error estimates or to estimate low-cloud feedbacks by separating regions.
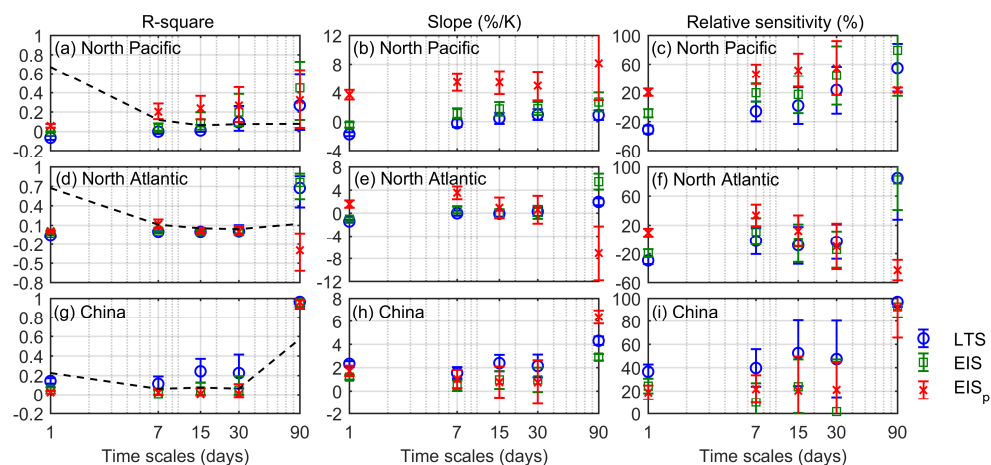
Figure 11. Similar to Fig. 10 but for the other three regions defined in Klein and Hartmann (1993), including two midlatitude oceans and one subtropical land.

515

Figs. 11a and 11d show that over the North Pacific and North Atlantic regions, variance from the daily time scale dominates (67%), while over the China region, variance from the seasonal time scale is the largest (57%, Fig.11g). Over the North Pacific and North Atlantic regions, LCC is not necessarily correlated with the IS. Norris (1998) has found that fogs and bad-weather stratus clouds frequently occur over the midlatitude ocean but with less inversions and poor IS-LCC relationships.

520   Similarly, poor correlation (Figs. 11a and 11d) and sensitivity (Figs. 11c and 11f) between LCC and LTS/EIS/EIS_p are found over the North Pacific and North Atlantic. But, the EIS_p is closest to the radiosonde-detected IS as compared with the LTS and EIS at the ENA and OWS C as shown in Table 2. This suggests that the EIS_p is still a reliable estimation for the IS to represent

the true IS-LCC relationship. But the LTS/EIS-LCC relationship is not necessarily due to the IS influence on LCC. Figs. 11a, 11d, 11c and 11f also show that the LTS/EIS-LCC correlation and sensitivity is very different from that between LCC and EIS_p on the daily and seasonal time scales. Unfortunately, limited knowledge about why this happen is known. The poor EIS_p-LCC relationship represents that the IS cannot be a cloud controlling factor as important as that over subtropical oceans. Over the Chinese region, the EIS and EIS_p are both better correlated with the IS as shown in Table 2. Fig. 11g and Fig. 11i shows that LCC is slightly more corelated with and sensitive to the LTS through all time scales. These higher correlations and sensitivity are not related to the IS since the LTS is the worst estimation for the IS. But it may imply that there are other thermal factors except the IS counted into LTS to contribute to these higher correlations and sensitivity. Overall, it should be noted that the IS may not be a strong cloud-controlling factor over the midlatitude oceans and subtropical land but EIS_p is still the best estimation for the IS.

All above analyses (Figs. 7-11) are based on the daily-averaged LTS, EIS and EIS_p data, which are computed based on the 3-hour 1° ERA5 atmospheric profiles. Based on the monthly mean atmospheric profiles, over the region of LCC larger than 60%, the LTS and EIS explain 50% and 48% of LCC variance, which is similar to the value of 53% based on the 3-hour ERA5 atmospheric profiles. However, the EIS_p based on the monthly mean ERA5 profiles explains 49% of the LCC variance, which is significantly lower than the 65% based on the 3-hour profiles. Thus for accurately computing the EIS_p on either short or long timescales, high temporal resolution of reanalysis data is necessary.

5. Conclusion

In this paper, a novel profile-based estimated IS (EIS_p) is developed based on the thinnest possible layer that contains the inversion layer in the ERA5 profiles. By this method, the effects of the static stability below the LCL are completely removed. The errors due to the spread of the environmental θ gradient around the moist adiabat above the LCL are reduced.

At the ARM SGP site, the EIS_p more accurately estimates the IS, with a correlation of 0.74, than the LTS (0.53) and EIS (0.45). Thus, the EIS_p reasonably replicates the constraints of IS on the PBL moisture distribution and LCC, while the LTS/EIS has a weak/wrong relationship with the PBL moisture and LCC. The LCC sensitivity to LTS and EIS and EIS_p is 39%, 12% and 50%, respectively. On the daily time scale (7-day mean excluded), the variance in LCC explained by the EIS_p (9.1%) is more than twice that explained by both the LTS (3.1%) and EIS (-0.4%). At the ARM ENA site, the EIS_p has similar advantages on estimating the IS. At other available oceanic and coastal observation stations, the EIS_p is still a better estimation for the IS than the LTS and EIS.

At the global scale, according to the GEO-MODIS LCC observations, the EIS_p better explains the spatial and temporal variations of LCC than the LTS and EIS. Over oceans, the EIS_p distribution is more consistent with the LCC pattern compared with the LTS and EIS. The locations of the strongest EIS_p are consistent with the centers of the largest LCC relatively away from the coast, while the centers of the strongest LTS and EIS are over the coast. Over the subtropical LCC domains, the LCC sensitivity to the EIS_p is 48%, larger than that to the LTS (37%) and EIS (36%) on all time scales. And the increased LCC sensitivity to EIS_p primarily comes from time scales shorter than a month. Over the typical low-cloud prevailing eastern oceans as defined in Klein and Hartmann (1993), the LCC daily variance explained by the EIS_p is 32% and twice that explained by the LTS/EIS. And the LCC seasonal variance explained by the EIS_p increases to 89% as compared with that explained by the LTS (80%) and EIS (70%).

No uniform relationship between the LCC and any of the IS, LTS, EIS and EIS_p is found across time scales or different regions. As compared to the LTS/EIS, the temporal relative variation of the LCC slopes to the EIS_p is reduced from 32%/29% to 21%. The regional relative variation of the LCC slope to the EIS_p is slightly smaller than that of LTS and EIS. This non-uniformness of the LCC sensitivity to the IS and three metrices suggests that the estimate of low cloud feedbacks based on a single observed relationship is questionable.

565 Overall, the EIS$_p$ is an improved measure of the IS and better constrains LCC, especially on time scales shorter than a month. On short time scales, the enhanced dependence of LCC on the EIS$_p$ makes the EIS$_p$ more suitable to resolve process-oriented studies associated with LCC variations. Therefore, the EIS$_p$ is likely a better constraint to reduce the meteorological covariations to separate the aerosol effects in aerosol-cloud interactions.

Author contribution.

570 JY and RW designed the experiments and ZW carried them out. JY and ZW prepared the first version of the manuscript with contributions from all co-authors. YC prepared the ERA5 data and TT inspected some individual profiles and cloud images. All authors verified the final version of the manuscript.

Competing interests.

The authors declare that they have no conflict of interest.

575 **Acknowledgment**

This work was supported by the NSFC-41875004 and the National Key R&D Program of China (2016YFC0202000). The first author thanks the "Double First-class" initiative program providing an opportunity for him to visit and study at the University of Washington.

Data Availability Statement

580 All data used in this study are available online. The ARM SGP radiosonde and cloud data were obtained from the ARM Research Facility and are available at https://www.arm.gov. The IGRA radiosondes are available from the NOAA National Centers for Environmental Information at https://www.ncei.noaa.gov/products/weather-balloon/integrated-global-radiosonde-archive. The GEO-MODIS LCC product is provided by the NASA Langley Research Center at https://earthdata.nasa.gov. The ERA5 reanalysis used in this study is from the ECMWF and available at https://cds.climate.copernicus.eu/cdsapp#!/home.

585

Reference

Albrecht, B. A., Jensen, M. P., and Syrett, W. J.: Marine boundary layer structure and fractional cloudiness, Journal of Geophysical Research, 100, 10.1029/95jd00827, 1995.

Bretherton, C. S., Widmann, M., Dymnikov, V. P., Wallace, J. M., and Bladé, I.: The Effective Number of Spatial Degrees of
590 Freedom of a Time-Varying Field, Journal of Climate, 12, 1990-2009, 10.1175/1520-0442(1999)012<1990:Tenosd>2.0.Co;2, 1999.

Bretherton, C. S., Uttal, T., Fairall, C. W., Yuter, S. E., Weller, R. A., Baumgardner, D., Comstock, K., Wood, R., and Raga, G. B.: The Epic 2001 Stratocumulus Study, Bulletin of the American Meteorological Society, 85, 967-978, 10.1175/bams-85-7-967, 2004.

595 Chen, X. and Xie, S.: ARM Best Estimate Data Products (ARMBECLDRAD), Atmospheric Radiation Measurement (ARM) user facility, 10.5439/1333228, 1996.

Coopman, Q., Garrett, T. J., Riedi, J., Eckhardt, S., and Stohl, A.: Effects of long-range aerosol transport on the microphysical properties of low-level liquid clouds in the Arctic, Atmospheric Chemistry and Physics, 16, 4661-4674, 10.5194/acp-16-4661-2016, 2016.

600 Doelling, D. R., Sun, M., Nguyen, L. T., Nordeen, M. L., Haney, C. O., Keyes, D. F., and Mlynczak, P. E.: Advances in Geostationary-Derived Longwave Fluxes for the CERES Synoptic (SYN1deg) Product, Journal of Atmospheric and Oceanic Technology, 33, 503-521, 10.1175/jtech-d-15-0147.1, 2016.

Doelling, D. R., Loeb, N. G., Keyes, D. F., Nordeen, M. L., Morstad, D., Nguyen, C., Wielicki, B. A., Young, D. F., and Sun, M.: Geostationary Enhanced Temporal Interpolation for CERES Flux Products %J Journal of Atmospheric and Oceanic Technology,

30, 1072-1090, 10.1175/jtech-d-12-00136.1, 2013.

Dong, X. Q., Minnis, P., and Xi, B. K.: A climatology of midlatitude continental clouds from the ARM SGP Central Facility: Part I: Low-level cloud macrophysical, microphysical, and radiative properties, Journal of Climate, 18, 1391-1410, Doi 10.1175/Jcli3342.1, 2005.

Durre, I., Vose, R. S., and Wuertz, D. B.: Overview of the Integrated Global Radiosonde Archive, Journal of Climate, 19, 53-68, Doi 10.1175/Jcli3594.1, 2006.

Durre, I., Yin, X., Vose, R. S., Applequist, S., and Arnfield, J.: Enhancing the Data Coverage in the Integrated Global Radiosonde Archive, Journal of Atmospheric and Oceanic Technology, 35, 1753-1770, 10.1175/jtech-d-17-0223.1, 2018.

Gryspeerdt, E., Quaas, J., and Bellouin, N.: Constraining the aerosol influence on cloud fraction, Journal of Geophysical Research: Atmospheres, 121, 3566-3583, 10.1002/2015jd023744, 2016.

Hersbach, H., Bell, B., Berrisford, P., Hirahara, S., Horányi, A., Muñoz-Sabater, J., Nicolas, J., Peubey, C., Radu, R., Schepers, D., Simmons, A., Soci, C., Abdalla, S., Abellan, X., Balsamo, G., Bechtold, P., Biavati, G., Bidlot, J., Bonavita, M., Chiara, G., Dahlgren, P., Dee, D., Diamantakis, M., Dragani, R., Flemming, J., Forbes, R., Fuentes, M., Geer, A., Haimberger, L., Healy, S., Hogan, R. J., Hólm, E., Janisková, M., Keeley, S., Laloyaux, P., Lopez, P., Lupu, C., Radnoti, G., Rosnay, P., Rozum, I., Vamborg, F., Villaume, S., and Thépaut, J. N.: The ERA5 global reanalysis, Quarterly Journal of the Royal Meteorological Society, 146, 1999-2049, 10.1002/qj.3803, 2020.

Jones, C. R., Bretherton, C. S., and Leon, D.: Coupled vs. decoupled boundary layers in VOCALS-REx, Atmospheric Chemistry and Physics, 11, 7143-7153, 10.5194/acp-11-7143-2011, 2011.

Kawai, H., Koshiro, T., and Webb, M. J.: Interpretation of Factors Controlling Low Cloud Cover and Low Cloud Feedback Using a Unified Predictive Index, Journal of Climate, 30, 9119-9131, 10.1175/jcli-d-16-0825.1, 2017.

Ken, B.: Balloon-Borne Sounding System (SONDEWNPN), Atmospheric Radiation Measurement (ARM) user facility, https://doi.org/10.5439/1595321, 2001.

Klein, S. A.: Synoptic Variability of Low-Cloud Properties and Meteorological Parameters in the Subtropical Trade Wind Boundary Layer, Journal of Climate, 10, 2018-2039, 10.1175/1520-0442(1997)010<2018:Svolcp>2.0.Co;2, 1997.

Klein, S. A. and Hartmann, D. L.: The Seasonal Cycle of Low Stratiform Clouds, Journal of Climate, 6, 1587-1606, 10.1175/1520-0442(1993)006<1587:Tscols>2.0.Co;2, 1993.

Klein, S. A., Hartmann, D. L., and Norris, J. R.: On the Relationships among Low-Cloud Structure, Sea Surface Temperature, and Atmospheric Circulation in the Summertime Northeast Pacific, Journal of Climate, 8, 1140-1155, 10.1175/1520-0442(1995)008<1140:Otralc>2.0.Co;2, 1995.

Klein, S. A., Hall, A., Norris, J. R., and Pincus, R.: Low-Cloud Feedbacks from Cloud-Controlling Factors: A Review, Surveys in Geophysics, 38, 1307-1329, 10.1007/s10712-017-9433-3, 2017.

L'Ecuyer, T. S., Berg, W., Haynes, J., Lebsock, M., and Takemura, T.: Global observations of aerosol impacts on precipitation occurrence in warm maritime clouds, Journal of Geophysical Research, 114, 10.1029/2008jd011273, 2009.

Li, J., Yi, Y., Minnis, P., Huang, J., Yan, H., Ma, Y., Wang, W., and Kirk Ayers, J.: Radiative effect differences between multi-layered and single-layer clouds derived from CERES, CALIPSO, and CloudSat data, Journal of Quantitative Spectroscopy and Radiative Transfer, 112, 361-375, 10.1016/j.jqsrt.2010.10.006, 2011.

Liu, S. Y. and Liang, X. Z.: Observed Diurnal Cycle Climatology of Planetary Boundary Layer Height, Journal of Climate, 23, 5790-5809, 10.1175/2010jcli3552.1, 2010.

Mauger, G. S. and Norris, J. R.: Meteorological bias in satellite estimates of aerosol-cloud relationships, Geophysical Research Letters, 34, 10.1029/2007gl029952, 2007.

Mauger, G. S. and Norris, J. R.: Assessing the Impact of Meteorological History on Subtropical Cloud Fraction, Journal of Climate, 23, 2926-2940, 10.1175/2010jcli3272.1, 2010.

McCoy, D. T., Eastman, R., Hartmann, D. L., and Wood, R.: The Change in Low Cloud Cover in a Warmed Climate Inferred from AIRS, MODIS, and ERA-Interim, Journal of Climate, 30, 3609-3620, 10.1175/jcli-d-15-0734.1, 2017.

Minnis, P., Trepte, Q. Z., Sun-Mack, S., Chen, Y., Doelling, D. R., Young, D. F., Spangenberg, D. A., Miller, W. F., Wielicki, B. A.,

650   Brown, R. R., Gibson, S. C., and Geier, E. B.: Cloud Detection in Nonpolar Regions for CERES Using TRMM VIRS and Terra and
        Aqua MODIS Data, IEEE Transactions on Geoscience and Remote Sensing, 46, 3857-3884, 10.1109/tgrs.2008.2001351, 2008.
        Minnis, P., Sun-Mack, S., Young, D. F., Heck, P. W., Garber, D. P., Chen, Y., Spangenberg, D. A., Arduini, R. F., Trepte, Q. Z., Smith,
        W. L., Ayers, J. K., Gibson, S. C., Miller, W. F., Hong, G., Chakrapani, V., Takano, Y., Liou, K.-N., Xie, Y., and Yang, P.: CERES Edition-
        2 Cloud Property Retrievals Using TRMM VIRS and Terra and Aqua MODIS Data—Part I: Algorithms, IEEE Transactions on
655   Geoscience and Remote Sensing, 49, 4374-4400, 10.1109/tgrs.2011.2144601, 2011.
        Mohrmann, J., Bretherton, C. S., McCoy, I. L., McGibbon, J., Wood, R., Ghate, V., Albrecht, B., Sarkar, M., Zuidema, P., and
        Palikonda, R.: Lagrangian Evolution of the Northeast Pacific Marine Boundary Layer Structure and Cloud during CSET, Monthly
        Weather Review, 147, 4681-4700, 10.1175/mwr-d-19-0053.1, 2019.
        Murray-Watson, R. J. and Gryspeerdt, E.: Stability-dependent increases in liquid water with droplet number in the Arctic,
660   Atmospheric Chemistry and Physics, 22, 5743-5756, 10.5194/acp-22-5743-2022, 2022.
        Myers, T. A. and Norris, J. R.: Observational Evidence That Enhanced Subsidence Reduces Subtropical Marine Boundary Layer
        Cloudiness, Journal of Climate, 26, 7507-7524, 10.1175/jcli-d-12-00736.1, 2013.
        Myers, T. A. and Norris, J. R.: Reducing the uncertainty in subtropical cloud feedback, Geophysical Research Letters, 43, 2144-
        2148, 10.1002/2015gl067416, 2016.
665   Myers, T. A., Scott, R. C., Zelinka, M. D., Klein, S. A., Norris, J. R., and Caldwell, P. M.: Observational constraints on low cloud
        feedback reduce uncertainty of climate sensitivity, Nature Climate Change, 11, 501-507, 10.1038/s41558-021-01039-0, 2021.
        Nicholls, S.: The dynamics of stratocumulus: Aircraft observations and comparisons with a mixed layer model, Quarterly
        Journal of the Royal Meteorological Society, 110, 783-820, 10.1002/qj.49711046603, 1984.
        Norris, J. R.: Low Cloud Type over the Ocean from Surface Observations. Part I: Relationship to Surface Meteorology and the
670   Vertical Distribution of Temperature and Moisture, Journal of Climate, 11, 369-382, 10.1175/1520-
        0442(1998)011<0369:Lctoto>2.0.Co;2, 1998.
        Qu, X., Hall, A., Klein, S. A., and Caldwell, P. M.: The strength of the tropical inversion and its response to climate change in 18
        CMIP5 models, Clim Dynam, 45, 375-396, 10.1007/s00382-014-2441-9, 2014.
        Romps, D. M.: Exact Expression for the Lifting Condensation Level, Journal of the Atmospheric Sciences, 74, 3891-3900,
675   10.1175/jas-d-17-0102.1, 2017.
        Rosenfeld, D., Zhu, Y., Wang, M., Zheng, Y., Goren, T., and Yu, S.: Aerosol-driven droplet concentrations dominate coverage
        and water of oceanic low-level clouds, Science, 363, 10.1126/science.aav0566, 2019.
        Schneider, T. and O'Gorman, P. A.: Moist Convection and the Thermal Stratification of the Extratropical Troposphere, Journal
        of the Atmospheric Sciences, 65, 3571-3583, 10.1175/2008jas2652.1, 2008.
680   Seethala, C., Norris, J. R., and Myers, T. A.: How Has Subtropical Stratocumulus and Associated Meteorology Changed since
        the 1980s?*, Journal of Climate, 28, 8396-8410, 10.1175/jcli-d-15-0120.1, 2015.
        Sherwood, S. C., Webb, M. J., Annan, J. D., Armour, K. C., Forster, P. M., Hargreaves, J. C., Hegerl, G., Klein, S. A., Marvel, K. D.,
        Rohling, E. J., Watanabe, M., Andrews, T., Braconnot, P., Bretherton, C. S., Foster, G. L., Hausfather, Z., von der Heydt, A. S.,
        Knutti, R., Mauritsen, T., Norris, J. R., Proistosescu, C., Rugenstein, M., Schmidt, G. A., Tokarska, K. B., and Zelinka, M. D.: An
685   Assessment of Earth's Climate Sensitivity Using Multiple Lines of Evidence, Rev Geophys, 58, e2019RG000678,
        10.1029/2019RG000678, 2020.
        Stevens, B. and Brenguier, J.-L.: Cloud-controlling factors: Low clouds, 2009.
        Stone, P. H.: A Simplified Radiative-Dynamical Model for the Static Stability of Rotating Atmospheres, Journal of the
        Atmospheric Sciences, 29, 405-418, 10.1175/1520-0469(1972)029<0405:Asrdmf>2.0.Co;2, 1972.
690   Szoeke, S. P., Verlinden, K. L., Yuter, S. E., and Mechem, D. B.: The Time Scales of Variability of Marine Low Clouds, Journal of
        Climate, 29, 6463-6481, 10.1175/jcli-d-15-0460.1, 2016.
        Trepte, Q. Z., Bedka, K. M., Chee, T. L., Minnis, P., Sun-Mack, S., Yost, C. R., Chen, Y., Jin, Z., Hong, G., Chang, F.-L., and Smith,
        W. L.: Global Cloud Detection for CERES Edition 4 Using Terra and Aqua MODIS Data, IEEE Transactions on Geoscience and
        Remote Sensing, 57, 9410-9449, 10.1109/tgrs.2019.2926620, 2019.

695   Webb, M. J., Lambert, F. H., and Gregory, J. M.: Origins of differences in climate sensitivity, forcing and feedback in climate
        models, Clim Dynam, 40, 677-707, 10.1007/s00382-012-1336-x, 2012.
        Wood, R. and Bretherton, C. S.: Boundary Layer Depth, Entrainment, and Decoupling in the Cloud-Capped Subtropical and
        Tropical Marine Boundary Layer, Journal of Climate, 17, 3576-3588, 10.1175/1520-0442(2004)017<3576:Bldead>2.0.Co;2,
        2004.
700   Wood, R. and Bretherton, C. S.: On the Relationship between Stratiform Low Cloud Cover and Lower-Tropospheric Stability,
        Journal of Climate, 19, 6425-6432, 10.1175/jcli3988.1, 2006.